The Astronomical Journal, 150:10 (18pp), 2015 July doi:10.1088/0004-6256/150/1/10
© 2015. The American Astronomical Society. All rights reserved.

WIYN OPEN CLUSTER STUDY. LXVI. SPECTROSCOPIC BINARY ORBITS IN THE YOUNG OPEN CLUSTER M35 (NGC 2168)

E. M. Leiner[1], R. D. Mathieu[1], N. M. Gosnell[2], and A. M. Geller[3,4]
[1] Department of Astronomy, University of Wisconsin—Madison, WI 53706, USA; leiner@astro.wisc.edu, mathieu@astro.wisc.edu
[2] Department of Astronomy, University of Texas at Austin, Austin, TX 78712, USA; gosnell@astro.as.utexas.edu
[3] Center for Interdisciplinary Exploration and Research in Astrophysics (CIERA) and Department of Physics and Astronomy, Northwestern University, 2145 Sheridan Rd, Evanston, IL 60208, USA
[4] Department of Astronomy and Astrophysics, University of Chicago, 5640 S. Ellis Avenue, Chicago, IL 60637, USA
Received 2015 January 6; accepted 2015 March 27; published 2015 June 18

ABSTRACT

The young (150 Myr) open cluster M35 (NGC 2168) has been one of the core clusters of the WIYN Open Cluster Study since 1997. Over these 17 years we have obtained approximately 8000 radial-velocity (RV) measurements of stars in the M35 field, which we provide here. Our target sample consists of 1355 photometrically selected stars in the field of M35 within the main sequence and binary sequence of the cluster and within $13 \leqslant V \leqslant 16.5$ and $(B - V) \geqslant 0.6$. Using our RV measurements we cleanly separate likely cluster members from field stars. We calculate RV membership probabilities for over 1200 stars in our sample. 418 are probable cluster members, of which 64 are velocity-variable (binary) systems. Here we present 52 orbital solutions for binary members of M35. This sample defines the hard binary population of M35 that dynamically powers the cluster. We also present *XMM-Newton* X-ray detections within the cluster. We use our large binary sample to search for interacting binaries among the X-ray sources, investigate M35's period–eccentricity distribution, and determine binary frequency. We find a circularization period of 9.9 ± 1.2 days and a binary frequency of 24% ± 3% for main-sequence binaries with $P < 10^4$ days. Determining these properties in a young cluster like M35 is key to defining the initial conditions used in models of cluster dynamical evolution.

Key words: binaries: spectroscopic – open clusters and associations: individual (M35 (NGC 2168))

Supporting material: machine-readable and VO tables

1. INTRODUCTION

M35 (NGC 2168) has been the subject of many studies, including our own ongoing WIYN Open Cluster Study (WOCS) for which we have been collecting radial-velocity (RV) data on solar-type stars in M35 for more than 15 years using the Hydra Multi-Object Spectrograph (MOS) at WIYN Observatory. M35 has been the subject of several photometric studies (Sung & Bessell 1999; von Hippel et al. 2002; Kalirai et al. 2003), proper-motion studies (Cudworth 1971; McNamara & Sekiguchi 1986; McNamara et al. 2011), studies of stellar rotation and tidal evolution in binary stars (Meibom & Mathieu 2005; Meibom et al. 2006, 2007), a study of X-ray sources (Gondoin 2013), abundance studies (Barrado y Navascués et al. 2001a; Steinhauer & Deliyannis 2004), an investigation of the mass function (Barrado y Navascués et al. 2001b), a search for variable stars in the field (Hu et al. 2005), and several studies of its white dwarf population (Williams et al. 2004, 2006, 2009). The first paper in this series, Geller et al. (2010), presented our initial radial-velocity membership study of M35, upon which we expand here. M35 has also recently been included in the new *Kepler* K2 mission (Howell et al. 2014), with 75 days of observations completed in early 2014 providing precision photometry covering much of the cluster.

M35 is a young open cluster centered at $\alpha = 06^{\mathrm{h}}09^{\mathrm{m}}07\overset{\mathrm{s}}{.}5$ and $\delta = +24°20'28''$. WOCS photometry establishes a distance to M35 of 805 ± 40 pc, with an age of 150 ± 25 Myr, a metallicity of [Fe/H] = −0.18 ± 0.05, and a reddening of $E(B - V) = 0.20 \pm 0.01$ (C. P. Deliyannis 2006, private communication; Sarrazine et al. 2000). The most recent published parameters provide a distance of 912^{+70}_{-65} pc and an age of 180 Myr using $E(B - V) = 0.20$ and [Fe/H] = −0.18 ± 0.05 (Kalirai et al. 2003). Note that these two studies used different sets of isochrones based on different stellar evolution models for their distance estimates. Leonard & Merritt (1989) use proper motions to derive a dynamical mass estimate for the cluster of between 1600 and 3200 $M_{\odot}$.

Because star clusters offer a coeval stellar sample, they provide an excellent means to study stellar and dynamical evolution. Binaries are of particular importance in these clusters. Not only can binaries merge or transfer mass to form non-standard stellar products such as blue stragglers (e.g., Geller & Mathieu 2011), the hard-binary population also dynamically powers the cluster. M35 offers a snap shot of a very young stellar population (150 Myr). Thus, understanding the binary population of M35 offers us insight into the initial cluster binary population, an important constraint for models of cluster dynamical evolution and non-standard star formation (Hurley et al. 2005; Geller et al. 2013).

Here we present orbital solutions for 80 binary systems identified by our RV study, 52 of which are cluster members. These binaries constitute a large sample of the hard-binary population of M35, ranging in periods from just a few days to on the order of 10^3 days. This sample allows us to investigate such properties and processes as hard-binary frequency, secondary-mass distributions, tidal interactions, and chromospheric activity. We also update the membership information and RV database originally presented in Geller et al. (2010), which now contains ~8000 observations of 1301 stars, up from 5201 observations of 1144 stars.

In Section 2 of this paper, we outline our stellar sample and observations. In Section 3 we present our full RV database and

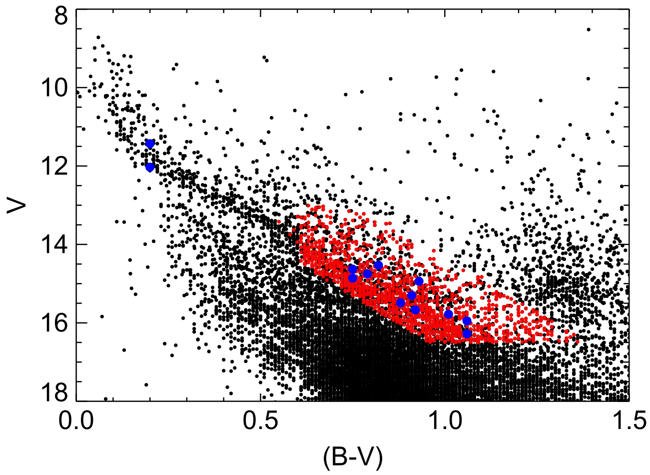

Figure 1. Color–magnitude diagram for stars in the M35 field. Black points are all stars in our initial photometry sample covering a 70′ × 70′ field around M35. Red points are stars that we have targeted for radial-velocity measurements. These points fall within our color–magnitude range and within 30′ of cluster center. Points plotted in blue indicate *XMM* X-ray sources.

reassess cluster membership for observed stars using this expanded sample. In Section 4, we present 80 orbital solutions for binaries discovered in our sample, 52 of which are cluster members. In Section 5 we present X-ray detections in our sample from *XMM-Newton* observations. In Sections 6 and 7 we discuss tidal circularization and binary frequency, two important properties of the cluster we can probe via our large binary sample.

2. WOCS SAMPLE AND OBSERVATIONS

2.1. Photometry and Target Selection

These binaries are drawn from a sample initially derived from the photometry of T. von Hippel taken at KPNO on the Burrell Schmidt telescope. Observations were taken on 1993 November 18–19, and include *B* and *V* photometry down to a magnitude of $V = 17$ lying within a 70′ × 70′ field of view. Subsequently, we updated this photometry for 74% of our sources with more precise *BV* photometry from C. P. Deliyannis (2006, private communication; Sarrazine et al. 2000). This new photometry was taken on the WIYN 0.9 m telescope with the S2KB imager and covers a 40′ × 40′ field of view. See Geller et al. (2010) for more information on these two sets of photometry.

From these photometric surveys, the WOCS target sample is selected based on magnitude, color, and radius from the cluster center. First, we select only stars covering the main sequence and binary sequence of M35 in color–magnitude space.[5] Our RV observations, taken at the WIYN 3.5 m using the Hydra MOS, have a limiting magnitude of $V = 16.5$. We impose a color cut, removing stars blueward of $(B - V) = 0.6$ ($[B - V]_0 = 0.4$) because a combination of scarce spectral lines and often rapid rotation impede our ability to measure precise radial velocities for these blue stars. Finally, we include only stars within 30 arcmin of the cluster center (~4 core radii, Mathieu 1983), a cutoff set by the radius of the Hydra MOS field.

[5] Specifically, stars between the lines defined by $V = 5.7(B - V) + 8.6$ and $V = 5.7(B - V) + 11.0$.

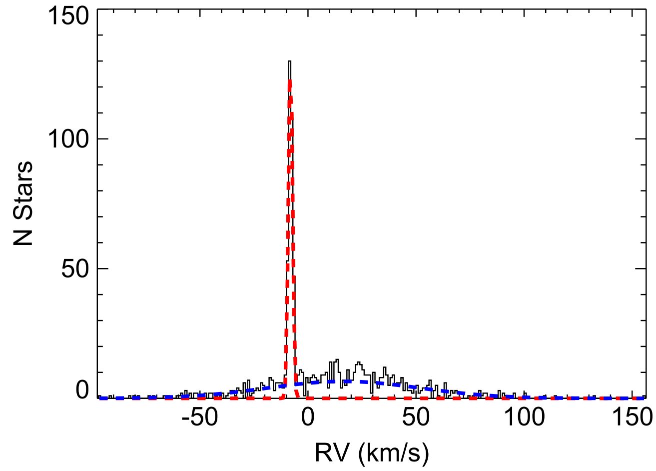

Figure 2. RV histogram for all non-RV-variable stars in the WOCS sample for M35. The dashed red line shows a Gaussian fit to the cluster RV distribution. The dashed blue line shows a Gaussian fit to the field RV distribution. Parameters of these fits are given in Table 1.

Table 1
Gaussian-fit Parameters for Cluster and Field RV Distributions

Parameter	Cluster	Field
Amplitude	130.5	7.0
$\overline{\mathrm{RV}}$ (km s^{-1})	−8.11	14.60
σ (km s^{-1})	0.95	31.99

Table 2
Membership Classifications for Stars in WOCS Sample of M35

Class	Number
SM	354
SN	694
BM	52
BN	28
BLM	12
BLN	93
BU	28
U	94

A color–magnitude diagram for all stars in the field of M35 is shown in Figure 1. WOCS target stars are plotted in red. The color–magnitude range of the WOCS targets corresponds to the M35 main sequence between 0.8 and 1.6 $M_\odot$ (Geller et al. 2010). The turnoff mass is 4.0 $M_\odot$, and thus both the upper and lower portion of the main sequence are excluded from our study.

Due to a photometry update, a few target stars that were formerly within our color–magnitude range no longer fall within these bounds. This includes three binary systems (2 members and one non-member). We have elected to publish these orbital solutions here anyway, and thus have retained them in our sample. However, we exclude these three stars from our binary frequency calculation in Section 7 so their inclusion will not impact our statistics. These appear as the three red points in Figure 1 bluewards of our color cut.

In addition, we have added X-ray sources in M35 from *XMM-Newton* observations (see Section 5). Two of these points fall outside our sample range in magnitude and color but are included for completeness. X-ray sources are plotted in

Table 3
Radial-velocity Data Table

ID_W	HJD—2,400,000 (days)	RV_1 (km s^{-1})	Correlation $Height_1$	$(O-C)_1$ (km s^{-1})	RV_2 (km s^{-1})	Correlation $Height_2$	$(O-C)_2$ (km s^{-1})	Phase
15010	…	…	…	…	…	…	…	…
	54873.781	27.8275	0.57	…	…	…	…	…
	54904.758	27.8172	0.87	…	…	…	…	…
	55136.931	31.0583	0.95	…	…	…	…	…
	55930.804	28.7873	0.95	…	…	…	…	…
	55958.656	27.9874	0.94	…	…	…	…	…
24013	…	…	…	…	…	…	…	…
	54904.758	58.0670	0.73	−0.05	…	…	…	0.092
	55137.827	59.0086	0.91	0.55	…	…	…	0.141
	55192.715	54.6878	0.91	−0.63	…	…	…	0.388
	55290.666	48.5153	0.91	0.06	…	…	…	0.829
	55467.955	52.3721	0.90	0.44	…	…	…	0.628
	55554.863	53.4827	0.92	−0.03	…	…	…	0.019
	55617.628	55.4943	0.92	−0.74	…	…	…	0.302
	55930.693	51.2247	0.93	0.42	…	…	…	0.711
	55958.656	46.7564	0.86	−0.73	…	…	…	0.837
	56272.877	57.1565	0.92	0.06	…	…	…	0.963
	56350.704	53.1481	0.91	0.00	…	…	…	0.252

(This table is available in its entirety in machine-readable and Virtual Observatory (VO) forms.)

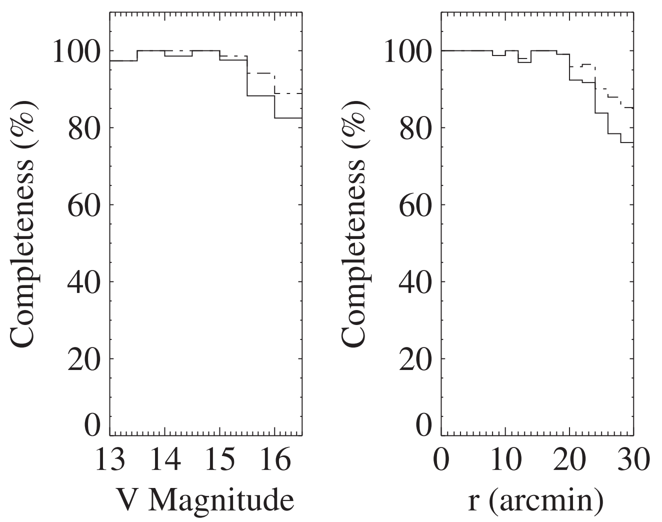

Figure 3. Completeness histogram showing the percentage of stars with at least 3 RV measurements (solid line) and 1 RV measurement (dashed line) as a function of apparent V-magnitude (left) and distance from cluster center (right).

Figure 1 in blue. These two targets are also excluded from our binary frequency calculation (see Section 7).

2.2. *Observations, Data Reduction, and Measurement Precision*

Beginning in 1997 September, we have obtained spectra for the stars in our sample at the WIYN 3.5 m telescope at KPNO using the Hydra MOS. For a detailed description of our observing and data reduction procedure see Geller et al. (2008). In short, we typically use Hydra's blue sensitive fibers and an echelle grating providing a resolution of $R\sim 20{,}000$. These spectra are centered on 512.5 nm, and span a ∼25 nm wavelength range, covering several prominent absorption lines including the MgB triplet. This setup has been occasionally altered over the years. For a description of alternate setups see Geller et al. (2010). For every science observation we also obtain one 100 s dome flat and two 300 s Thorium–Argon comparison spectra for calibration. We split our science observations into three equal-length integrations (three 20 minute exposures for stars with $V\leqslant 15.5$ and three 40 minute exposures for stars with $15.5 > V$) for cosmic ray rejection.

Every spectrum is bias subtracted, dispersion corrected, flat-fielded, throughput corrected, and sky subtracted using IRAF. We then cross-correlate the resulting spectra with a solar template spectrum. The resulting cross correlation function (CCF) is fit with a Gaussian to obtain a radial velocity. For single-lined stars we use a one-dimensional CCF. RVs for our double-lined observations are determined using TODCOR, a two-dimensional correlation routine developed by Mazeh & Zucker (1994). Using TODCOR we can determine RVs simultaneously for both the primary and secondary component of a double-lined system, even for observations that appear highly blended in the 1D CCF. We define a "good" observation as having a CCF peak height of at least 0.4 (or for spectra with multiple peaks, a primary CCF peak of at least 0.4), and do not use any observations yielding a lower peak height (Geller et al. 2008).

As a young cluster, M35 contains stars with a broad range of rotational velocities. Our RV measurement precision for narrow-lined stars is 0.5 km s^{-1}, but worsens for rapidly rotating stars with broad spectral features (Geller et al. 2010). Large rotational velocities broaden the CCF peaks to widths exceeding our spectral resolution and degrade the precision of our RV measurements.

Geller et al. (2010) provide a linear relationship between the $v\sin i$ of a star and our RV precision:

$$\sigma_i = 0.38 + 0.012(v\ \sin\ i)\ \mathrm{km\ s^{-1}} \tag{1}$$

In brief, Geller et al. (2010) measure the $v\sin i$ in the method of Rhode et al. (2001); they Doppler broaden our standard solar template with a series of theoretical rotational velocities, producing a set of artificially broadened template spectra. They

Table 4
Radial-velocity Summary Table

ID_W	ID_G	ID_M	ID_{Mc}	ID_C	R.A. (J2000)	Decl. (J2000)	V	$B-V$	S[a]	N_{obs}	$\overline{RV}$ (km s^{-1})	$\overline{RV_e}$ (km s^{-1})	σ_i	$\overline{v \sin i}$ (km s^{-1})	$\overline{v \sin i_e}$ (km s^{-1})	P_{RV}	P_{PM1}	P_{PM2}	e/i	Class	Comment
6006	6006	…	231	…	6 08 59.47	24 18 36.40	13.16	0.69	2	44	−7.66	3.738	0.94	46.3	0.4	96	99	…	3.99	SM	RR
90049	83049	…	…	…	6 07 25.86	24 14 5.60	16.27	1.16	2	3	43.42	0.753	0.53	12.5	3.5	0	…	…	1.42	SN	…
30035	30035	…	…	…	6 08 36.44	24 04 53.10	14.75	0.73	2	34	−7.36	8.875	0.60	18.1	0.4	96	…	…	14.86	BM	SB1
20020	20020	…	…	…	6 09 9.71	24 29 59.80	14.07	0.61	2	6	−8.49	0.752	0.60	18.5	0.7	96	…	…	1.25	SM	…
31038	31038	196	…	…	6 08 24.75	24 04 41.20	14.76	0.68	2	3	−8.55	0.544	0.56	15.0	0.3	96	…	…	0.97	SM	…
11029	11029	…	…	676	6 09 58.86	24 28 46.10	13.42	0.55	2	24	1.55	6.669	1.39	84.4	8.8	0	…	14	4.79	BN	SB1, RR
25024	25024	160	…	…	6 09 33.12	24 30 41.10	15.60	0.94	2	8	−9.54	1.504	0.69	25.9	0.7	90	…	…	2.18	SM	RR
19040	20040	…	…	…	6 10 32.68	24 16 56.50	14.26	0.67	1	3	−17.60	0.339	0.62	20.3	0.9	0	…	…	0.54	SN	RR
14052	17052	…	…	…	6 10 17.53	24 40 57.60	14.10	0.83	1	3	−20.99	0.620	0.50	10	0	0	…	…	1.24	SN	…
68041	60041	…	…	…	6 08 46.81	24 40 24.60	15.48	0.78	1	5	23.28	2.144	0.50	10	0	0	…	…	4.29	BLN	SB1
26032	26032	…	…	…	6 07 59.40	24 20 8.80	14.71	0.67	2	4	12.70	1.025	0.50	10.3	0.20	0	…	…	2.05	SN	…

Note.
[a] Photometry source. 1 = original Burrell Schmidt photometry. 2 = Updated photometry from C.P. Deliyannis.

(This table is available in its entirety in machine-readable and Virtual Observatory (VO) forms.)

Table 5
Orbital Parameters for M35 Single-lined Binaries

ID	P (days)	Orbital Cycles	γ (km s^{-1})	K (km s^{-1})	e	ω (deg)	$T_\circ$ (HJD-2400000 d)	$a \sin i$ (10^6 km)	$f(m)$ ($M_\odot$)	σ (km s^{-1})	N
4003	4430	1.3	−8.59	4.61	0.311	168.1	54337.67	267	3.8e-2	0.39	29
	±50	…	±0.08	±0.12	±0.019	±1.2	±0.06	±7	±0.3e-2	…	…
7003	643.9	8.0	−9.1	12.8	0.25	206.0	52775.03	109	1.26e-1	1.19	17
	±1.1	…	±0.3	±0.5	±0.04	±1.2	±0.06	±4	±1.4e-2	…	…
7025	361.9	15.6	−9.0	7.2	0.14	151.2	53916.07	36	1.4e-2	1.12	29
	±0.9	…	±1.4	±1.7	±0.08	±1.2	±0.06	±8	±1.0e-2	…	…
9003	804.5	7.9	−7.2	7.5	0.66	196.9	54347.50	62	1.5e-2	1.31	29
	±1.4	…	±0.3	±0.6	±0.04	±1.2	±0.06	±6	±0.4e-2	…	…
9016	41.201	52.4	−10.30	16.23	0.372	260.2	56034.51	8.53	1.46e-2	0.48	18
	±0.007	…	±0.12	±0.22	±0.013	±1.2	±0.06	±0.13	±0.6e-3	…	…
10019	1155	4.5	−8.6	7.7	0.703	140	53844.9	86	1.9e-2	0.88	42
	±4	…	±0.3	±0.9	±0.023	±40	±1.0	±11	±0.7e-2	…	…
12059	144.9	17.5	−9.0	5.3	0.39	27.1	55467.38	9.7	1.7e-3	0.70	16
	±0.3	…	±0.3	±0.8	±0.06	±1.9	±0.07	±1.5	±0.8e-3	…	…
14025	22.6190	275.0	−7.85	17.47	0.398	290	52603.6	4.99	9.7e-3	0.50	20
	±0.0003	…	±0.14	±0.21	±0.010	±30	±0.3	±0.06	±0.4e-3	…	…
15012	23.275	224.6	−8.7	12	0.71	186	53192.9	2.7	1.4e-3	3.29	31
	±0.004	…	±0.7	±6	±0.15	±10	±0.5	±1.6	±2.3e-3	…	…
16016	7.08858	756.5	−7.49	30.18	0.005	83.7	52731.20	2.942	2.02e-2	0.42	18
	±0.00005	…	±0.11	±0.15	±0.006	±1.6	±0.06	±0.014	±0.3e-3	…	…
16025	935.3	5.6	−7.20	8.7	0.15	360	54190	110	6.1e-2	0.82	24
	±2.3	…	±0.17	±0.3	±0.04	±10	±30	±4	±0.6e-2	…	…
18012	358.0	16.3	−8.95	2.93	0.32	242.1	52942.9	13.7	7.9e-4	0.84	34
	±0.7	…	±0.20	±0.23	±0.07	±1.2	±0.3	±1.1	±1.9e-4	…	…
18016	79.186	75.0	−8.24	15.10	0.378	329.2	52179.08	15.22	2.24e-2	0.45	21
	±0.007	…	±0.12	±0.16	±0.010	±1.8	±0.07	±0.17	±0.7e-3	…	…
19057	1129	4.5	−9.2	8	0.83	104.1	54075.50	70	1.1e-2	1.15	30
	±10	…	±0.3	±3	±0.09	±0.9	±0.07	±30	±1.2e-2	…	…
20016	49.0732	121.6	−9.34	16.81	0.351	249.9	52126.652	10.62	1.98e-2	0.45	32
	±0.0021	…	±0.10	±0.18	±0.013	±0.5	±0.024	±0.13	±0.7e-3	…	…
23023	649.6	8.3	−6.45	-17.1	0.794	148.5	54750.25	−92	−7.5e-2	1.53	52
	±0.3	…	±0.22	±1.6	±0.024	±0.9	±0.06	±10	±-2.2e-2	…	…
23043	7.7609	606.4	−6.66	10.0	0.03	35	53897.0	1.07	8.1e-4	1.06	25
	±0.0004	…	±0.22	±0.4	±0.03	±6	±0.3	±0.04	±0.9e-4	…	…
24014	344.5	15.2	−6.72	4.32	0.34	124.1	51885.40	19.2	2.4e-3	0.43	19
	±0.9	…	±0.14	±0.15	±0.04	±1.2	±0.06	±0.7	±0.3e-3	…	…
24023	30.1335	169.2	−7.58	28.19	0.273	332.0	51893.21	11.24	6.23e-2	0.37	19
	±0.0010	…	±0.11	±0.22	±0.004	±1.2	±0.06	±0.09	±1.5e-3	…	…
26030	456.5	13.1	−7.41	8.30	0.50	234.3	53018.84	45.3	1.78e-2	0.67	24
	±0.3	…	±0.16	±0.23	±0.03	±1.2	±0.06	±1.5	±1.6e-3	…	…
27026	474.7	12.3	−7.12	5.92	0.496	28.7	52199.82	33.6	6.7e-3	0.42	20
	±0.5	…	±0.10	±0.14	±0.018	±1.2	±0.06	±0.9	±0.5e-3	…	…
28007	156.94	23.5	−6.8	18.6	0.58	97.3	52591.96	32.9	5.7e-2	1.67	24
	±0.09	…	±0.4	±0.7	±0.03	±1.2	±0.06	±1.5	±0.7e-2	…	…
29022	2210	2.6	−8.24	2.63	0.17	236.4	53566.24	79	4.0e-3	0.74	25
	±50	…	±0.15	±0.24	±0.09	±1.2	±0.06	±7	±1.1e-3	…	…
30035	1036.59	5.7	−7.51	21	0.889	292.6	53223.98	136	9.0e-2	0.49	34
	±0.22	…	±0.14	±3	±0.021	±1.2	±0.06	±21	±0.4e-1	…	…
31009	792	6.6	−8.8	8.0	0.28	91.0	52119.89	83	3.7e-2	0.68	19
	±8	…	±0.4	±0.3	±0.06	±1.2	±0.06	±4	±0.4e-2	…	…
33043	473.9	11.4	−7.15	6.66	0.39	85.9	53021.59	39.9	1.13e-2	0.45	20
	±0.9	…	±0.11	±0.20	±0.03	±1.2	±0.06	±1.3	±1.0e-3	…	…
33054	11.7706	389.0	−6.1	45.5	0.208	196.1	53338.64	7.20	1.08e-1	1.49	19
	±0.0003	…	±0.4	±0.6	±0.013	±1.2	±0.06	±0.10	±0.4e-2	…	…
34036	12.283942	514.4	−7.35	25.30	0.554	93.9	52718.38	3.558	1.190e-2	0.32	26
	±0.000022	…	±0.07	±0.11	±0.003	±1.2	±0.06	±0.018	±1.7e-4	…	…
35042	959.8	6.0	−7.35	10.1	0.53	117.8	53139.11	113	6.3e-2	0.89	25
	±1.2	…	±0.20	±0.5	±0.03	±1.2	±0.06	±7	±1.0e-2	…	…
35045	10.07719	536.5	−9.20	49.86	0.004	84.4	52616.70	6.91	1.290e-1	0.70	20
	±0.00005	…	±0.18	±0.24	±0.005	±1.2	±0.06	±0.03	±1.9e-3	…	…
37029	45.1211	107.5	−7.27	22.7	0.237	102.4	55658.88	13.67	5.00e-2	0.48	20
	±0.0024	…	±0.14	±0.3	±0.013	±1.2	±0.06	±0.19	±2.0e-3	…	…

Table 5
(Continued)

ID	P (days)	Orbital Cycles	γ (km s^{-1})	K (km s^{-1})	e	ω (deg)	$T_\circ$ (HJD-2400000 d)	$a \sin i$ (10^6 km)	$f(m)$ ($M_\odot$)	σ (km s^{-1})	N
40015	10.33029	566.0	−7.37	40.5	0.016	69.1	51776.66	5.75	7.09e-2	0.82	24
	±0.00009	…	±0.23	±0.3	±0.007	±1.2	±0.06	±0.04	±1.3e-3	…	…
41026	6100	1.0	−7.48	3.75	0.12	110.0	54713.53	312	3.2e-2	0.41	35
	±110	…	±0.07	±0.12	±0.03	±1.2	±0.06	±10	±0.3e-2	…	…
41032	14.5198	360.0	−6.0	21.4	0.10	350.5	52843.82	4.26	1.46e-2	3.21	41
	±0.0009	…	±0.6	±0.8	±0.03	±1.2	±0.06	±0.16	±1.6e-3	…	…
42034	70.02	83.9	−7.55	3.30	0.14	150.4	54960.61	3.14	2.5e-4	0.43	19
	±0.03	…	±0.11	±0.15	±0.05	±1.2	±0.06	±0.14	±0.3e-4	…	…
43040	1344	2.2	−7.77	7.25	0.241	345.3	54923.80	129.9	4.84e-2	0.32	17
	±5	…	±0.08	±0.12	±0.015	±1.2	±0.06	±2.2	±2.4e-3	…	…
49043	12.5661	143.2	−8.35	23.3	0.097	45.9	52270.58	4.00	1.62e-2	0.69	17
	±0.0005	…	±0.18	±0.3	±0.010	±1.2	±0.06	±0.04	±0.5e-3	…	…
51013	153.30	35.8	−7.8	15.9	0.39	326.3	54360.84	31.0	5.0e-2	1.47	19
	±0.10	…	±0.4	±0.6	±0.03	±1.2	±0.06	±1.2	±0.6e-2	…	…
54027	2.2471731	2111.2	−8.07	46.13	−0.003	162.1	52958.77	1.425	2.29e-2	0.59	20
	±0.0000020	…	±0.13	±0.21	±0.004	±1.2	±0.06	±0.006	±0.3e-3	…	…
54054	8.01310	722.3	−8.52	8.26	0.039	350.9	53402.53	0.909	4.7e-4	0.56	21
	±0.00010	…	±0.13	±0.21	±0.024	±1.2	±0.06	±0.023	±0.4e-4	…	…
59018	18.4267	283.6	−6.9	37.4	0.292	325.8	52669.61	9.06	8.7e-2	1.12	22
	±0.0009	…	±0.3	±0.4	±0.010	±1.2	±0.06	±0.10	±0.3e-2	…	…
77033	2690	2.2	−5.80	6.4	0.48	102.9	54432.48	206	4.8e-2	0.93	24
	±40	…	±0.20	±0.3	±0.04	±1.2	±0.06	±12	±0.8e-2	…	…
97044	862	4.7	−8.05	3.4	0.44	88.5	55821.07	36	2.5e-3	0.65	18
	±4	…	±0.16	±0.3	±0.08	±1.2	±0.06	±4	±0.7e-3	…	…

then cross-correlate these broadened templates with the original narrow-lined solar template and measure the FWHM and peak height of the resulting CCF. This is done for a variety of rotation speeds to produce a function relating FWHM to $v \sin i$. Geller et al. (2010) then perform a precision analysis in three $v \sin i$ "bins," and fit a linear function to these precision values (Equation (1)).

Thus, our quoted precision of 0.5 km s^{-1} for M35 holds for the narrow-lined stars with $v \sin i \leqslant 10.0$ km s^{-1}. This corresponds to a FWHM of ∼45 km s^{-1}. For stars with $v \sin i > 10.0$ km s^{-1} we compute a precision for each star, adopting any average $v \sin i$ measurements made by Geller et al. (2010). For those stars newly presented here, we compute the $v \sin i$ for each measurement using the same method, and then average them for each star. These values are listed in Table 4. We then compute the precision from this average $v \sin i$ using Equation (1).

2.3. Membership Determination

With at least three RV measurements we can determine whether a star is velocity variable, which indicates a binary or higher order system. We define a velocity-variable star to have at least 3 RV measurements with a standard deviation ($\sigma_{\rm RV}$) greater than 4 times the measurement precision ($e/i \geqslant 4$) for that star.[6]

Once we have obtained at least 3 RV measurements for a non-velocity-variable star we evaluate its probability of M35 membership. For velocity-variable stars, we require more observations in order to determine an orbital solution and center-of-mass velocity for the system before we can make a secure membership determination. For a detailed description of our methodology and initial M35 membership determinations see Geller et al. (2010). Here we reapply the technique to our sample, which has grown substantially more complete since the previous publication, providing us with secure memberships for 315 new stars and 1128 stars overall.

2.3.1. RV Membership Probability

Figure 2 shows a histogram of RVs for non-velocity-variable stars ($e/i < 4$) with three or more observations. Here we include only stars with $\sigma_{\rm RV} < 2.0$ km s^{-1}.

Plotted in Figure 2 in red and blue are simultaneous Gaussian fits to the cluster velocity distribution and field velocity distribution, respectively. Parameters for the Gaussian fits are given in Table 1 and are consistent with the parameters derived in Geller et al. (2010). Using the prescription of Geller et al. (2010) we can determine RV membership probability using the equation:

$$P_{\rm RV}(v) = \frac{F_{\rm c}(v)}{F_{\rm f}(v) + F_{\rm c}(v)} \quad (2)$$

where $F_{\rm c}$ is the value of the Gaussian fit to the cluster velocity distribution and $F_{\rm f}$ is the fit to the field velocity distribution.

For very rapidly rotating stars, membership probabilities calculated in this way will be less reliable due to their poorer RV measurement precision. Because of this, we repeated the process outlined above using Gaussian fits to a RV histogram including only the most rapidly rotating stars ($20 < v \sin i < 80$ km s^{-1}) with $e/i < 4$. We used these fits to calculate revised membership probabilities for all 204 of the fastest rotators in our sample ($v \sin i > 20$). In most cases the membership probabilities calculated in this way differed only slightly from the membership probabilities calculated from the Gaussian fits in Table 1. Only in one case did this difference result in a

[6] Measurement precision is calculated based on a star's $v \sin i$. See Section 2.2 for details.

Table 6
Orbital Parameters for Field Single-lined Binaries

ID	P (days)	Orbital Cycles	γ (km s^{-1})	K (km s^{-1})	e	ω (deg)	$T_\circ$ (HJD-2400000 d)	$a \sin i$ (10^6 km)	$f(m)$ ($M_\odot$)	σ (km s^{-1})	N
11029	392.4	12.4	2.70	15	0.88	66.0	53052.37	40	2.0e-2	0.63	19
	±1.0	…	±0.19	±10	±0.11	±1.2	±0.06	±30	±0.3e-1	…	…
16026	555.2	5.3	−2.55	10.67	0.304	4	55159.5	77.6	6.0e-2	0.38	14
	±0.8	…	±0.12	±0.15	±0.014	±30	±0.3	±1.1	±0.3e-2	…	…
18019	153.3	7.9	47.41	4.1	0.49	219	55785.2	7.5	7.1e-4	0.32	10
	±0.5	…	±0.20	±0.4	±0.05	±3	±0.3	±0.8	±2.1e-4	…	…
18044	18.8594	114.9	17.23	26.17	0.176	101.0	54576.8	6.68	3.34e-2	0.44	12
	±0.0005	…	±0.14	±0.22	±0.008	±1.2	±0.3	±0.06	±0.9e-3	…	…
24013	222.1	6.5	52.60	8.5	0.67	247	55550.7	19.2	5.8e-3	0.65	12
	±1.5	…	±0.21	±0.5	±0.04	±6	±0.3	±1.6	±1.2e-3	…	…
34038	1337	1.1	−26.38	6.34	0.11	90.3	56391.14	116	3.5e-2	0.39	11
	±19	…	±0.13	±0.21	±0.03	±1.2	±0.06	±4	±0.3e-2	…	…
35038	58.124	83.6	0.92	12.69	0.143	163.2	54417.22	10.04	1.19e-2	0.38	14
	±0.009	…	±0.18	±0.13	±0.015	±1.2	±0.06	±0.11	±0.4e-3	…	…
36032	2610	1.7	−4.0	19	0.94	285.8	54880.14	200	8.0e-2	0.87	32
	±30	…	±0.5	±21	±0.12	±1.2	±0.06	±300	±0.3e 0	…	…
41013	4.6153	179.3	−0.6	21.4	0.029	46.9	51257.83	1.36	4.7e-3	1.16	18
	±0.0003	…	±0.3	±0.4	±0.022	±1.2	±0.06	±0.03	±0.3e-3	…	…
41020	8.17003	466.9	−5.1	32.4	0.598	338.8	52286.54	2.92	1.48e-2	2.09	48
	±0.00014	…	±0.3	±0.9	±0.014	±1.2	±0.06	±0.09	±1.3e-3	…	…
42042	12.2171	90.3	26.6	40.8	0.321	220.6	52694.06	6.50	7.32e-2	0.68	12
	±0.0003	…	±0.3	±0.4	±0.007	±1.2	±0.06	±0.07	±2.1e-3	…	…
45038	8.07448	145.5	−0.24	29.93	0.146	88.4	51289.96	3.287	2.17e-2	0.51	19
	±0.00021	…	±0.13	±0.17	±0.006	±1.2	±0.06	±0.019	±0.4e-3	…	…
46036	1507	3.4	−5.3	18	0.92	83.8	54416.08	150	5.6e-2	0.58	32
	±5	…	±0.7	±15	±0.11	±1.2	±0.06	±150	±1.5e-1	…	…
66038	252.7	20.2	40.78	3.42	0.36	188.8	54461.95	11.1	8.5e-4	0.44	10
	±0.3	…	±0.16	±0.23	±0.06	±1.2	±0.06	±0.8	±1.7e-4	…	…
72047	8.27032	403.4	15.41	37.7	0.014	307.4	55127.89	4.29	4.60e-2	1.03	21
	±0.00012	…	±0.25	±0.3	±0.009	±1.2	±0.06	±0.04	±1.1e-3	…	…
75047	97.037	34.4	17.83	16.0	0.209	134.5	54831.89	20.8	3.82e-2	0.86	16
	±0.023	…	±0.24	±0.3	±0.021	±1.2	±0.06	±0.4	±2.2e-3	…	…
77050	4.243697	510.6	3.89	46.6	0.011	207.8	54973.98	2.721	4.46e-2	0.76	20
	±0.000023	…	±0.21	±0.3	±0.007	±1.2	±0.06	±0.016	±0.8e-3	…	…
81034	68.581	64.2	−1.39	19.2	0.016	150.9	54071.43	18.1	5.06e-2	0.91	21
	±0.010	…	±0.22	±0.3	±0.017	±1.2	±0.06	±0.3	±2.1e-3	…	…
91048	14.3866	176.7	4.14	29.0	0.014	222.4	54671.23	5.73	3.62e-2	0.83	20
	±0.0009	…	±0.23	±0.3	±0.012	±1.2	±0.06	±0.05	±1.0e-3	…	…

change to a star's membership classification (WOCS 27015 changed from a nonmember to a member).

2.3.2. Membership Classification

Membership classification for the velocity variables (binary or higher order systems) is complicated by the need to obtain center-of-mass velocities to accurately gauge membership probability, and thus requires an orbital solution which may not yet be available. Thus, Hole et al. (2009) introduced a classification scheme that is useful if orbital solutions have not yet been determined for all velocity-variable stars in a sample. Following Geller et al. (2010), we split our sample into eight possible classifications defined as follows.

1. *Single Member (SM):* velocity-non-variable stars ($e/i < 4$) with $P_{\rm RV} \geqslant 50\%$ (using Equation (1)).
2. *Single Nonmember (SN):* velocity-non-variable stars ($e/i < 4$) with $P_{\rm RV} < 50\%$ (using Equation (1)).
3. *Binary Member (BM):* velocity-variable stars ($e/i \geqslant 4$) for which we have orbital solutions. BMs have $P_{\rm RV} \geqslant 50\%$ using the center-of-mass velocity (γ) to determine membership probability.
4. *Binary Nonmember (BN):* velocity-variable stars ($e/i \geqslant 4$) for which we have orbital solutions. BNs have $P_{\rm RV} < 50\%$ using the γ-RV to determine membership probability.
5. *Binary Likely Member (BLM):* velocity-variable stars ($e/i \geqslant 4$) for which we do not have orbital solutions. BLMs have $P_{\rm RV} \geqslant 50\%$ based on their average RV. Because we do not yet have completed solutions, this classification is more uncertain than BM and subject to change.
6. *Binary Likely Nonmember (BLN):* velocity-variable stars ($e/i \geqslant 4$) for which we do not have orbital solutions. BLNs have $P_{\rm RV} < 50\%$ based on their average RV and the range of RV measurements for the star do not include the cluster mean. Because we do not yet have completed solutions, this classification is more uncertain than BN and subject to change.
7. *Binary Unknown (BU):* velocity-variable stars ($e/i \geqslant 4$) for which we do not have orbital solutions. BUs have $P_{\rm RV} < 50\%$ but the range of RV measurements for the star do include the cluster mean.

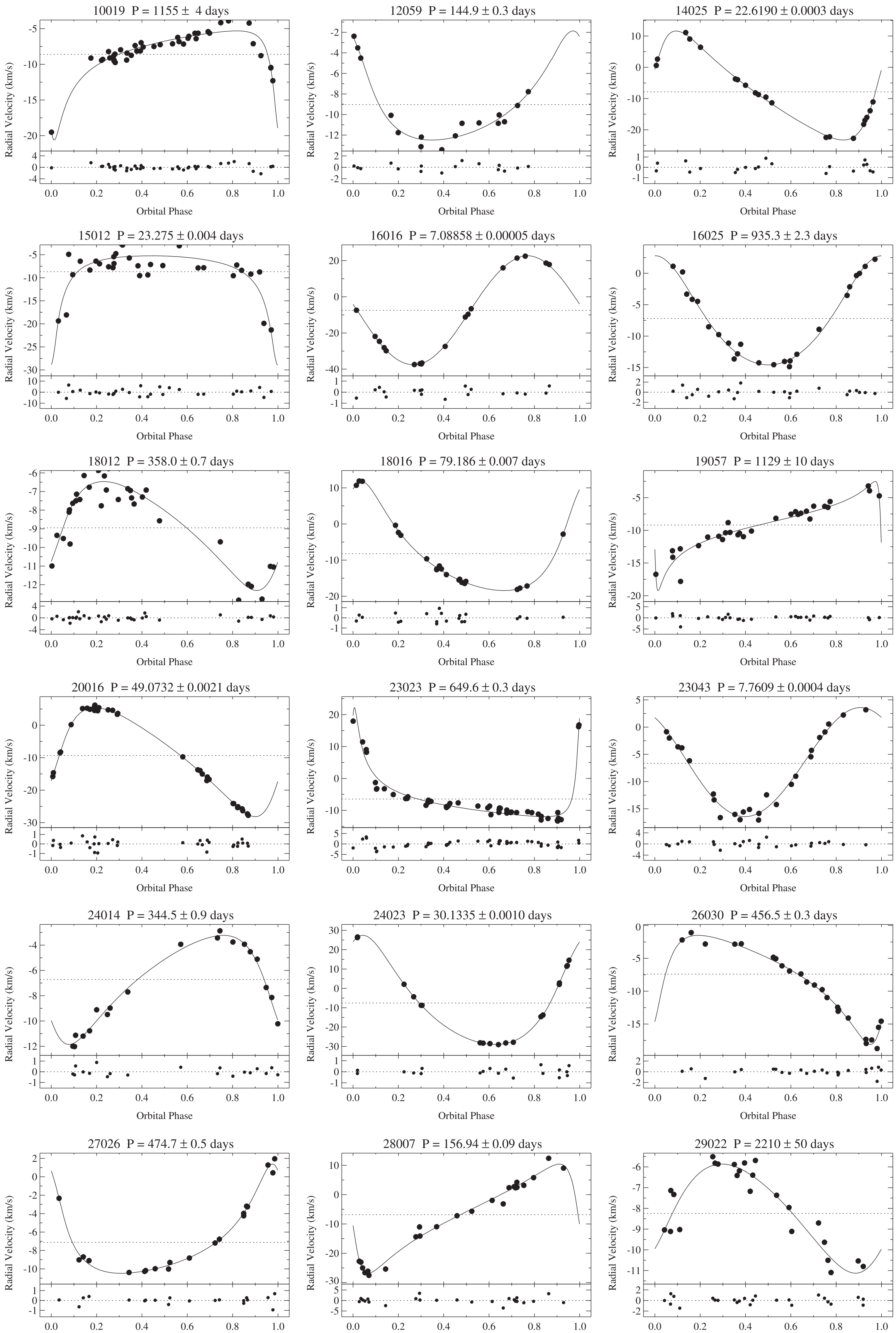

Figure 4. M35 SB1 orbit plots. For each binary, we plot RV against orbital phase, showing the data points with filled circles and the orbital fit to the data with the solid line. The dotted line marks the γ-velocity. Beneath each orbit plot, we show the residuals $(O-C)$ from the fit. Above each plot, we give the binary ID and orbital period.

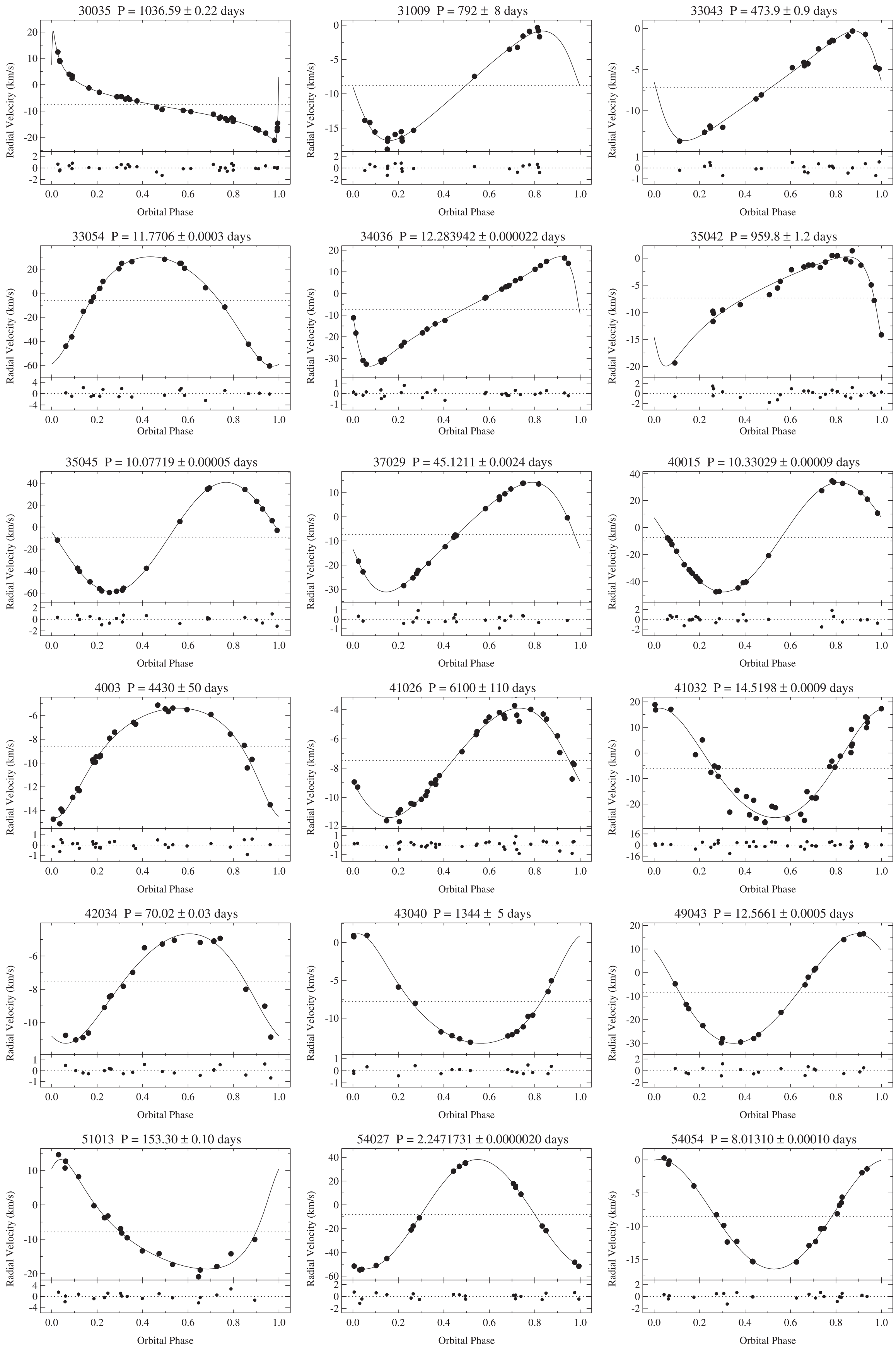

Figure 4. (Continued.)

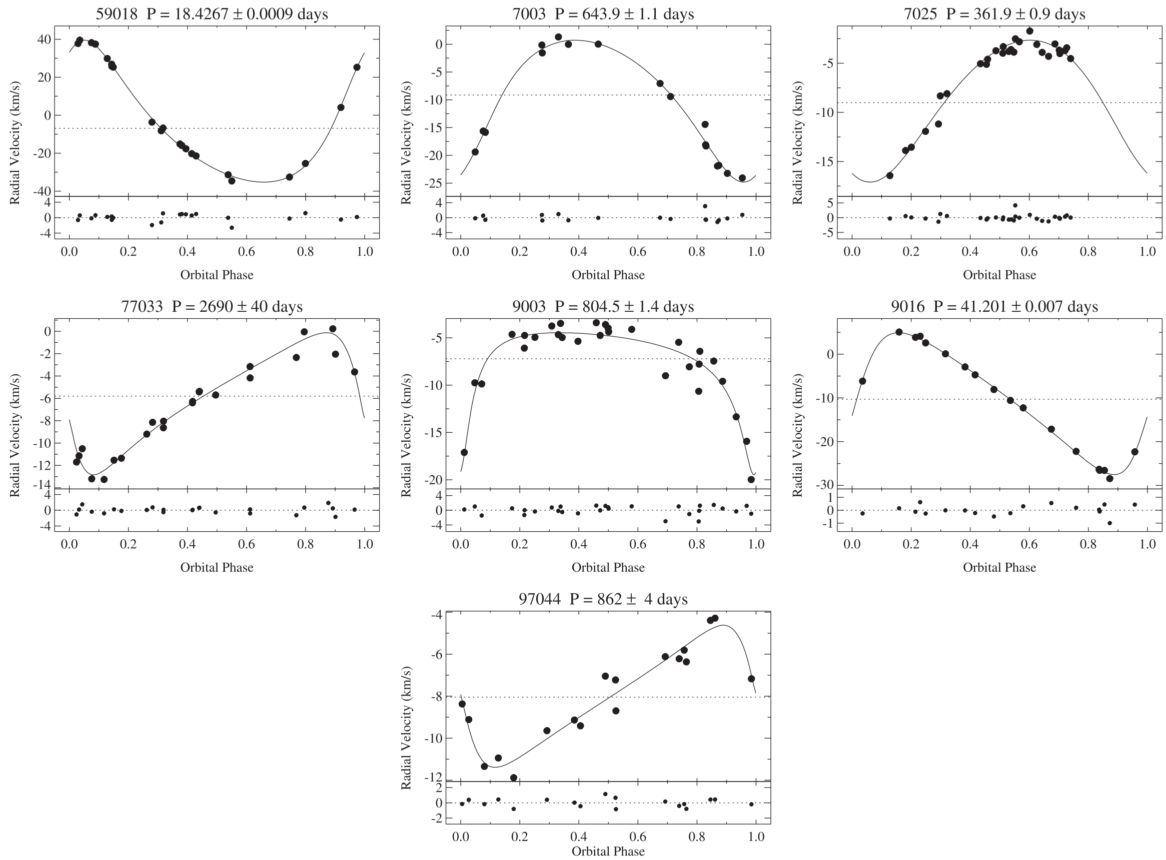

Figure 4. (Continued.)

8. *Unknown (U):* stars that have <3 RV measurements, along with stars such as rapid rotators for which we are unable to derive accurate RVs from our spectra.

Table 2 gives the census of membership classification of our sample. Note that we report unobserved stars in our sample as U's. This is a change from the classification in Geller et al. (2010), who do not report a classification for unobserved stars and do not include them in their tables.

Note that the cutoff for membership at $P_{\rm RV} = 50\%$ was chosen by Geller et al. (2010) because it cleanly separates the membership probability distributions of members and non-members. (See Figure 7 of Geller et al. 2010, a histogram of RV membership probabilities for the cluster.) Using this cutoff results in an expected 6% field star contamination (Geller et al. 2010). The proper-motion memberships cover only a small fraction of the stars in our sample, but where they overlap we find good agreement with our memberships. Of the 77 RV members in our sample with proper-motion memberships, 72 (94%) are also found to be proper-motion members ($P_{\rm PM} \geqslant 50\%$) by McNamara & Sekiguchi (1986).

3. RV MEASUREMENTS

We present here all RV measurements of the 1355 stars in our sample to date, totaling ~8000 RVs. A table of all our RV measurements is presented electronically. In Table 3 we present two entries to show the table's content: one single-lined (SB1) binary and one single star. The table lists WOCS ID (ID), the date of the observation (HJD), the RV of the CCF peak (RV_1), and the CCF peak height (Correlation Height_1) for all measurements. In the case that the star is a binary with an orbital solution we list the residual $(O-C)_1$ derived as the observed minus expected RV based on the solution, as well as the orbital phase of the observation. In the case that the star is a double-lined binary (SB2), we also list the secondary RV (RV_2), CCF height (Correlation Height_2), and residual $(O-C)_2$.

1301 stars out of 1355 have been observed at least once, for a completeness of 96% across our sample. 1261 stars (93%) have ⩾3 RV measurements. Overall, 83% of our sample (1128 stars) have enough observations to be considered complete and their membership status final. For these stars we either have ⩾3 RV measurements that show no velocity variability, or, if we do observe them to be velocity variable we have sufficient observations to determine an orbital solution. These stars comprise the SM, SN, BM, and BN categories.

Figure 3 shows the completeness of our observations for stars with ⩾1 RV measurement (dotted line), and ⩾3 RV measurements (solid line). The histograms show completeness as a function of apparent *V*-magnitude (left) and radius from cluster center (right). Completeness nears 100% for brighter stars and stars near the center of the cluster. Only fainter stars ($V > 15.5$) near the edges of the WOCS field show some incompleteness because we prioritize stars closer to cluster center for observations.

Note that WOCS IDs have changed since the publication of Geller et al. (2010). The WOCS ID system is numbered based on radial distance from the cluster center and *V*-magnitude (see Hole et al. 2009). Due to a photometry update the magnitudes of some stars were revised, and we have now renumbered these

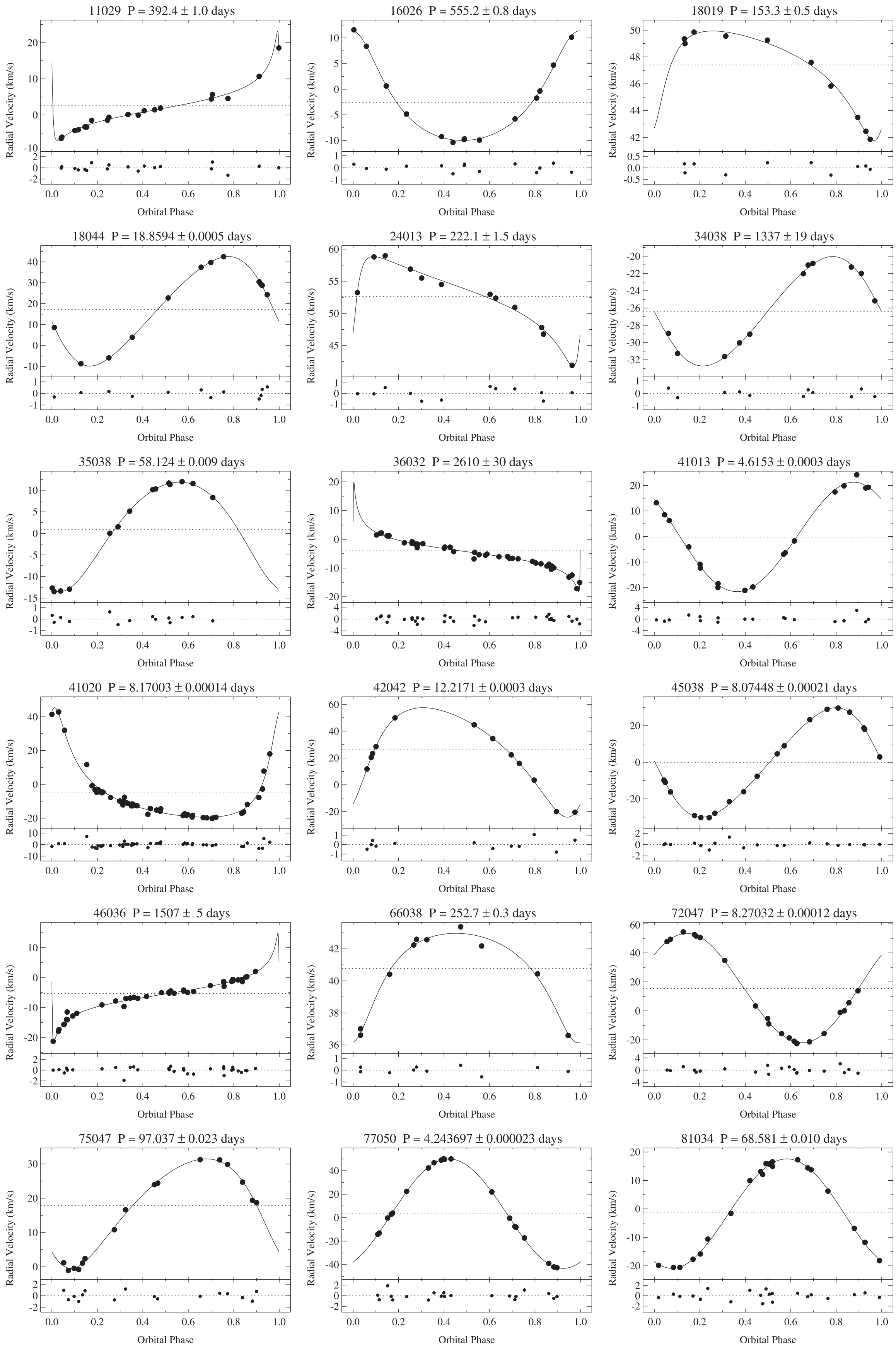

Figure 5. Non-member SB1 orbit plots. For each binary, we plot RV against orbital phase, showing the data points with filled circles and the orbital fit to the data with the solid line. The dotted line marks the γ-velocity. Beneath each orbit plot, we show the residuals from the fit. Above each plot, we give the binary ID and orbital period.

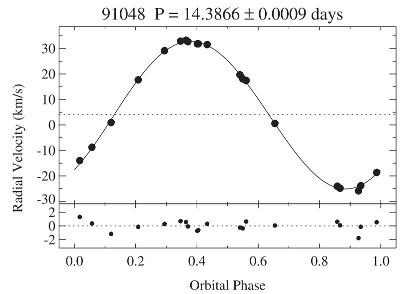

Figure 5. (Continued.)

WOCS IDs to remain faithful to the magnitude-based numbering system. The current WOCS ID and the WOCS ID from Geller et al. (2010) are therefore different for some stars.

Table 4 provides a summary of results for each star in our sample. The table lists the current WOCS ID ($\mathrm{ID_W}$), $\mathrm{ID_G}$ (ID from Geller et al. 2010), $\mathrm{ID_M}$ (Meibom et al. 2009), $\mathrm{ID_{Mc}}$ (McNamara & Sekiguchi 1986), $\mathrm{ID_C}$ (Cudworth 1971), J2000 R.A. and decl., V-band apparent magnitude (V), color ($B - V$), the source of the photometry (S), number of observations (N_{obs}), average radial-velocity ($\overline{\mathrm{RV}}$), standard deviation of the radial velocity measurements ($\overline{\mathrm{RV}_e}$), measurement precision (σ_i), average $v \sin i$ value ($\overline{v \sin i}$), standard error on the mean $v \sin i$ ($\overline{v \sin i_e}$), RV membership probability calculated with Equation (2) (P_{RV}), proper-motion membership probability from McNamara & Sekiguchi (1986) (P_{PM1}) or Cudworth (1971) (P_{PM2}), ratio of the RV standard deviation to the single measurement precision (e/i), the membership classification (Class) according to the scheme outlined in Section 2.3.2, and a comment indicating whether the star is an SB1, SB2, X-ray source, etc.

Note that we are not able to accurately measure projected rotation velocities of 10 km s^{-1} or less due to our spectral resolution. Thus, any star with a $v \sin i$ of 10 km s^{-1} or slower is denoted in Table 4 as having a $v \sin i$ of 10 km s^{-1} with 0 km s^{-1} error. Also note that for SB2 stars, the $v \sin i$ value listed is for the primary CCF peak, and blending of the two peaks in many cases results in larger uncertainties and an inflated $v \sin i$ value. Finally, note that the version of this table included in Geller et al. (2010) in some cases lists the incorrect $\mathrm{ID_M}$, which has been corrected here.

4. SPECTROSCOPIC BINARY ORBITAL SOLUTIONS

Using the same procedure outlined in Geller et al. (2009), we can fit an orbital solution to RV measurements of velocity-variable stars, provided we have a sufficient number of observations. Here we present orbital solutions for 80 binaries. Most of these solutions are secure. For a few very high eccentricity orbits the phase coverage is less complete, and thus these solutions merit caution. 52 of these 80 binaries are cluster members and 28 are non-members according to the membership criteria given in Section 2.3.

4.1. Single-lined Binaries

Single-lined binaries (SB1s) are velocity-variable stars with only one distinguishable CCF peak in our correlation spectra.

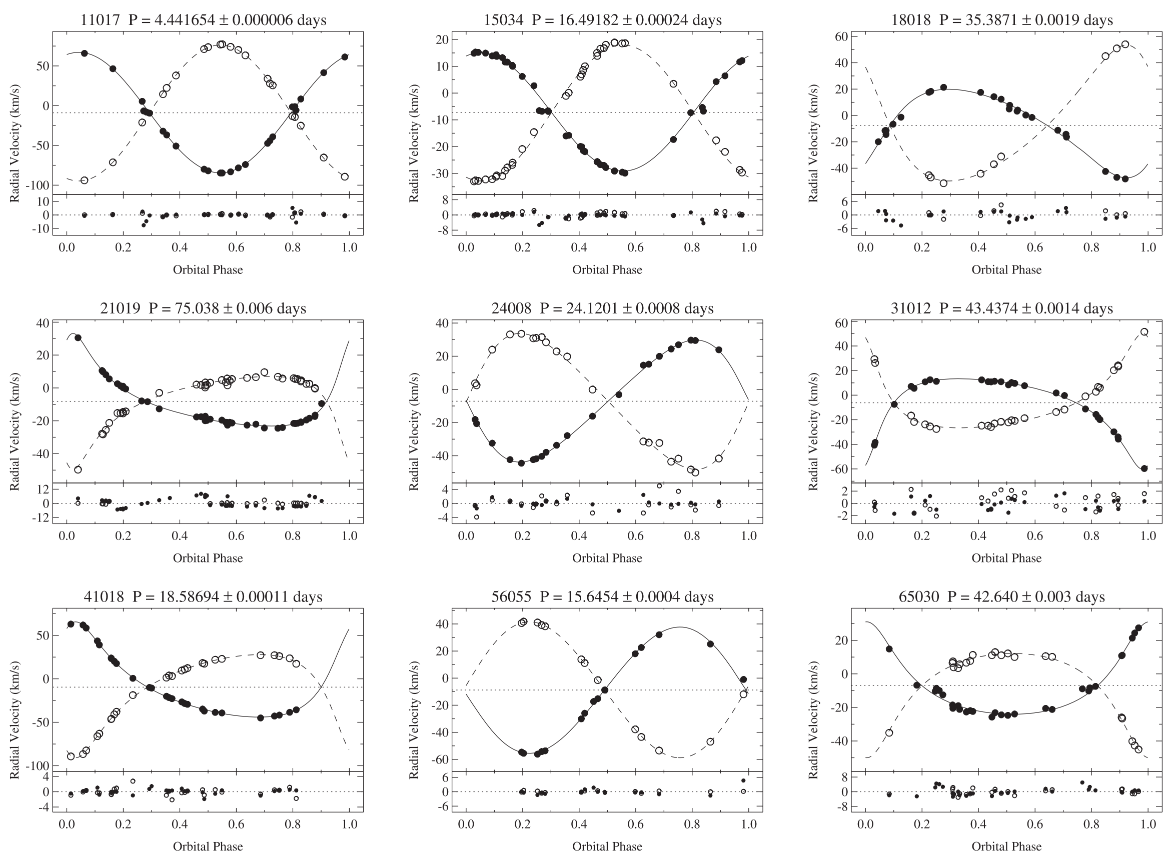

Figure 6. M35 SB2 orbit plots. For each binary, we plot RV against orbital phase, showing the primary-star data points with filled circles and the secondary-star data points with open circles. The orbital fits to the data are plotted in the solid and dashed lines for the primary and secondary stars, respectively. The dotted line marks the γ-velocity. Beneath each orbit plot, we show the residuals from the fit. Above each plot, we give the binary ID and orbital period.

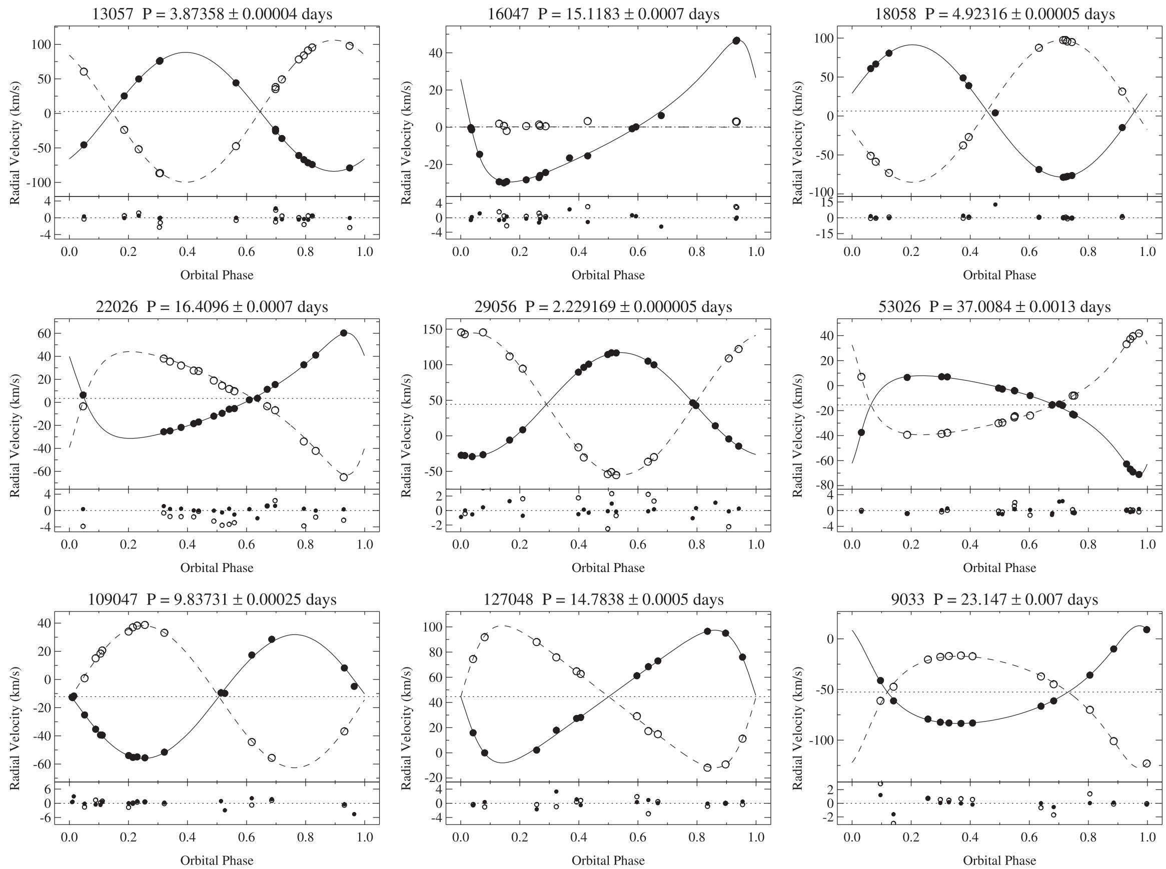

Figure 7. Non-member SB2 orbit plots. For each binary, we plot RV against orbital phase, showing the primary-star data points with filled circles and the secondary-star data points with open circles. The orbital fits to the data are plotted in the solid and dashed lines for the primary and secondary stars, respectively. The dotted line marks the γ-velocity. Beneath each orbital plot, we show the residuals from the fit. Above each plot, we give the binary ID and orbital period.

Orbital solutions fit to our RV measurements are listed in Tables 5 and 6 for singled-lined members and non-members respectively. For each star we list the WOCS ID, orbital period (P), the number of orbital cycles encompassed by our measurements, the center-of-mass velocity (γ), orbital amplitude (K), eccentricity (e), longitude of periastron (ω), Julian date of periastron (T_0), projected semi-major axis ($a \sin i$), mass function ($f(m)$), RMS residual velocity of the orbital solution (σ), and the number of RV measurements (N). Orbital solutions for each of our SB1s are plotted in Figures 4 and 5 for members and non-members, respectively.

4.2. Double-lined Binaries

SB2s are those velocity-variable stars with two distinguishable CCF peaks in our correlation spectra. For these stars we have RV measurements for both the primary and the secondary stars. Orbital solutions for these systems are plotted in Figures 6 and 7 for members and non-members, respectively. Parameters for these orbital solutions for both the primary and secondary stars are listed in Tables 7 (cluster members) and 8 (non-members). The parameters listed are the same as in Tables 5 and 6, but instead of listing a mass function ($f(m)$) we give $m^3 \sin(i)$ for each star as well as the mass ratio, q.

Note that WOCS 16047, a non-member ($P_{\rm RV} = 0$) SB2 binary, is a triple system. It displays two clear CCF peaks. The primary peak yields a solution for a binary system with an orbital period of 15 days. The secondary peak appears nearly stationary across observations, consistent with being a wide tertiary companion with a long orbital period. Table 8 gives the orbital solution for the primary binary.

5. X-RAY COUNTERPARTS USING *XMM-NEWTON*

5.1. Observations and Data Reduction

M35 was observed in the X-ray by the *XMM-Newton* orbiting observatory for 8.6 ks (02:37:10–05:00:50 UT) on 2008 September 20. The telescope boresight location was $6^{\rm h}8^{\rm m}54^{\rm s}$, $+24°20'00''$ (J2000). The *XMM* field of view with $r = 15'$ does not extend as far from cluster center as the WOCS RV survey ($r = 30'$, $\alpha = 06^{\rm h}09^{\rm m}07\overset{\rm s}{.}5$, $\delta = +24°20'28''$).

We use *XMM* Science Analysis Software (SAS) version 13.5 for our data analysis efforts, whereas previous studies (Gondoin 2013) relied on pipeline-produced products and the source list from the *XMM* Serendipitous Source Catalog (Watson et al. 2009).

An ultraviolet image of M35 was taken concurrently with the X-ray data using the Optical Monitor (OM) instrument aboard *XMM* with a field of view of $17' \times 17'$. We reduce the UVM2 (200–220 nm) image using the SAS pipeline routine omichain. This output includes a list of 478 sources with corresponding position information and aperture photometry. Comparing the OM source positions with positions in the WOCS catalog reveals no systematic offsets. Therefore we do not correct the telescope boresight position in our further analysis.

We do not find any flaring during the observation, so we retain the entire exposure for source detection. We filter the

Table 7
Orbital Parameters for M35 Double-lined Binaries

ID	P (days)	Orbital Cycles	γ (km s^{-1})	K (km s^{-1})	e	ω (deg)	$T_\circ$ (HJD-2400000 d)	$a \sin i$ (10^6 km)	$m \sin^3 i$ ($M_\odot$)	q	σ (km s^{-1})	N
11017	4.441654	1243.0	−8.96	75.8	0.003	344.5	51812.61	4.63	1.024	0.887	2.69	25
	±0.000006	…	±0.23	±0.8	±0.003	±1.2	±0.06	±0.06	±0.015	±0.012	…	…
	…	…	…	85.5	…	…	…	5.222	0.908	…	1.04	21
	…	…	…	±0.4	…	…	…	±0.024	±0.022	…	…	…
15034	16.49182	361.2	−7.22	22.1	0.009	340.8	52974.98	5.01	0.098	0.871	1.53	41
	±0.00024	…	±0.16	±0.3	±0.010	±1.2	±0.06	±0.08	±0.003	±0.016	…	…
	…	…	…	25.4	…	…	…	5.76	0.085	…	1.17	34
	…	…	…	±0.3	…	…	…	±0.07	±0.003	…	…	…
18018	35.3871	138.5	−7.6	33.7	0.272	227.5	52812.01	15.8	1.22	0.653	2.17	24
	±0.0019	…	±0.4	±0.8	±0.020	±1.2	±0.06	±0.4	±0.06	±0.021	…	…
	…	…	…	51.6	…	…	…	24.1	0.80	…	2.13	9
	…	…	…	±0.9	…	…	…	±0.5	±0.04	…	…	…
21019	75.038	69.5	−8.13	28.2	0.543	329.0	52702.20	24.4	0.414	0.998	1.23	42
	±0.006	…	±0.15	±0.6	±0.010	±1.2	±0.06	±0.5	±0.020	±0.023	…	…
	…	…	…	28.3	…	…	…	24.5	0.413	…	1.29	38
	…	…	…	±0.6	…	…	…	±0.5	±0.019	…	…	…
24008	24.1201	211.3	−7.12	36.8	0.195	89.2	52059.53	11.97	0.584	0.898	1.07	21
	±0.0008	…	±0.22	±0.3	±0.009	±1.2	±0.06	±0.12	±0.022	±0.018	…	…
	…	…	…	41.0	…	…	…	13.33	0.525	…	2.27	20
	…	…	…	±0.7	…	…	…	±0.23	±0.014	…	…	…
31012	43.4374	77.4	−6.22	36.8	0.515	204.3	52758.81	18.87	0.616	0.960	1.01	27
	±0.0014	…	±0.16	±0.4	±0.006	±1.2	±0.06	±0.21	±0.020	±0.016	…	…
	…	…	…	38.4	…	…	…	19.7	0.591	…	1.41	26
	…	…	…	±0.6	…	…	…	±0.3	±0.016	…	…	…
41018	18.58694	291.7	−9.55	54.8	0.431	329.2	52736.33	12.65	1.093	0.925	0.73	27
	±0.00011	…	±0.12	±0.3	±0.004	±1.2	±0.06	±0.06	±0.015	±0.007	…	…
	…	…	…	59.3	…	…	…	13.68	1.010	…	1.03	25
	…	…	…	±0.3	…	…	…	±0.08	±0.012	…	…	…
56055	15.6454	188.6	−8.78	46.6	0.051	93.6	55686.32	10.02	0.760	0.929	1.64	16
	±0.0004	…	±0.13	±0.6	±0.004	±1.2	±0.06	±0.16	±0.015	±0.014	…	…
	…	…	…	50.19	…	…	…	10.78	0.706	…	0.42	13
	…	…	…	±0.25	…	…	…	±0.06	±0.023	…	…	…
65030	42.640	103.9	−7.0	27.5	0.383	356.5	53572.93	14.9	0.37	0.89	2.18	30
	±0.003	…	±0.3	±0.9	±0.019	±1.2	±0.06	±0.5	±0.03	±0.03	…	…
	…	…	…	31.1	…	…	…	16.8	0.33	…	1.56	21
	…	…	…	±0.9	…	…	…	±0.5	±0.03	…	…	…

event lists for the pn and two MOS cameras to include only those events with energies between 0.2–12 keV and 0.3–12 keV for the MOS and pn cameras, respectively. Images for each camera are created from the filtered event lists using the EVSELECT task in three bandpasses of 0.2–1.0, 1.0–7.5, and 7.5–12.0 keV (the soft-band pn image is 0.3–1.0 keV). We run the EDETECT_CHAIN task on pn, MOS1, and MOS2 images in all three bands simultaneously. We find a combined source list of 41 X-ray sources in the central field of M35.

We cross-correlate the position of each X-ray source with the WOCS catalog to find potential optical counterparts to the X-ray sources. We classify a WOCS object as a potential optical counterpart to an X-ray source if the WOCS position agrees with the X-ray position to 2σ, given the X-ray position error, and if the total separation is less than 4.″0. Modeling by Gondoin (2013) shows that beyond 4.″0, the number of spurious optical counterpart matches continues to increase while the number of reliable counterpart matches has reached its maximum. The X-ray position error is found by combining in quadrature the 1σ error calculated using the EML_DETECT task within EDETECT_CHAIN and the 1.″0 systematic error assumed by the *XMM* Serendipitous Source Catalog (Watson et al. 2009). Using this cross-correlation technique we find 17 optical counterparts to X-ray sources in M35: 12 cluster members, 4 non-members and one whose membership is unknown. The 12 members and 1 source of unknown membership (13 sources total) comprise our X-ray sample of M35, and each X-ray source has only one potential optical counterpart. Two of these 13 sources lie outside the color–magnitude limits of our main RV sample but are included for completeness.

We follow the strategy of van den Berg et al. (2013) to estimate the likelihood of random overlap of a WOCS catalog object and an X-ray source. We split our analysis between inside the core radius (7.′5, Mathieu 1983) and outside the core radius, as the projected density of optical sources decreases with cluster radius. Within the core radius the density of WOCS objects is 0.00023 sources arcsec^2. Outside of the core radius but within the *XMM* field of view the WOCS object density is 0.00017 sources arcsec^2. We calculate the total area covered by the 2σ X-ray position error circles in each region and find the X-ray source coverage to be 998.47 arcsec^2 inside the core radius and 1750.24 arcsec^2 outside the core radius. This results in an expected number of random matches of 0.2 and 0.3 sources inside and outside of the core radius, respectively. As a conservative estimate we conclude that in total one X-ray counterpart match may be false.

Table 8
Orbital Parameters for Field Double-lined Binaries

ID	P (days)	Orbital Cycles	γ (km s^{-1})	K (km s^{-1})	e	ω (deg)	$T_\circ$ (HJD-2400000 d)	$a \sin i$ (10^6 km)	$m \sin^3 i$ ($M_\odot$)	q	σ (km s^{-1})	N
9033	23.147	18.1	−52.53	48.3	0.394	24.9	55322.16	14.12	1.10	0.876	0.77	12
	±0.007	…	±0.24	±0.5	±0.013	±1.2	±0.06	±0.14	±0.04	±0.017	…	…
	…	…	…	55.1	…	…	…	16.1	0.96	…	1.68	12
	…	…	…	±0.9	…	…	…	±0.3	±0.03	…	…	…
13057	3.87358	190.5	2.66	86.2	0.006	217.8	54349.39	4.591	1.477	0.837	0.78	14
	±0.00004	…	±0.20	±0.4	±0.005	±1.2	±0.06	±0.022	±0.022	±0.007	…	…
	…	…	…	102.9	…	…	…	5.48	1.237	…	1.42	14
	…	…	…	±0.6	…	…	…	±0.04	±0.015	…	…	…
16047	15.1183	117.4	0.1	38.2	0.492	63.2	52903.45	6.91	…	…	1.17	18
	±0.0007	…	±0.3	±0.5	±0.019	±1.2	±0.06	±0.10	…	…	…	…
	…	…	…	0.1	…	…	…	…	…	…	2.23	10
	…	…	…	±0.9	…	…	…	…	…	…	…	…
18058	4.92316	174.2	6.36	84.9	0.009	285.4	55612.09	5.74	1.44	0.931	4.47	12
	±0.00005	…	±0.21	±1.7	±0.004	±1.2	±0.06	±0.14	±0.04	±0.023	…	…
	…	…	…	91.2	…	…	…	6.17	1.34	…	0.65	11
	…	…	…	±0.5	…	…	…	±0.04	±0.07	…	…	…
22026	16.4096	109.5	3.40	45.8	0.436	56.3	55772.56	9.30	0.66	0.86	0.84	17
	±0.0007	…	±0.25	±0.8	±0.012	±1.2	±0.06	±0.14	±0.05	±0.03	…	…
	…	…	…	53.6	…	…	…	10.9	0.56	…	2.80	15
	…	…	…	±1.6	…	…	…	±0.3	±0.03	…	…	…
29056	2.229169	878.2	44.40	72.92	0.004	165.2	55110.15	2.235	0.690	0.730	0.70	19
	±0.000005	…	±0.17	±0.21	±0.003	±1.2	±0.06	±0.007	±0.016	±0.008	…	…
	…	…	…	99.9	…	…	…	3.06	0.503	…	2.98	14
	…	…	…	±1.0	…	…	…	±0.03	±0.007	…	…	…
53026	37.0084	127.6	−15.40	39.7	0.540	220.2	52537.86	17.03	0.604	0.975	1.03	19
	±0.0013	…	±0.17	±0.4	±0.007	±1.2	±0.06	±0.19	±0.013	±0.013	…	…
	…	…	…	40.8	…	…	…	17.46	0.589	…	0.83	15
	…	…	…	±0.4	…	…	…	±0.15	±0.014	…	…	…
109047	9.83731	226.3	−12.2	44.0	0.020	87.7	55003.87	5.95	0.457	0.873	1.89	18
	±0.00025	…	±0.3	±0.9	±0.010	±1.2	±0.06	±0.14	±0.020	±0.020	…	…
	…	…	…	50.4	…	…	…	6.82	0.399	…	1.11	12
	…	…	…	±0.7	…	…	…	±0.10	±0.020	…	…	…
127048	14.7838	200.3	44.6	52.7	0.352	89.8	55365.11	10.03	0.84	0.934	1.41	12
	±0.0005	…	±0.3	±0.6	±0.006	±1.2	±0.06	±0.15	±0.03	±0.018	…	…
	…	…	…	56.4	…	…	…	10.74	0.79	…	1.38	12
	…	…	…	±0.6	…	…	…	±0.15	±0.03	…	…	…

Table 9
X-ray Sources with Cluster Member Optical Counterparts

XMM ID	WOCS ID	V	$B-V$	Dist. (arcsec)	X_{err} (arcsec)	PL Index[a]	$L_X \times 10^{30}$ (erg s^{-1})[b]	$\overline{v \sin i}$ (km s^{-1})	Class
XMMUJ 060825.6+242336	6021	12.03	0.20	1.66	2.10	$2.8^{+0.3}_{-0.3}$	6.1 ± 0.5	36.9 ± 1.3	BU
XMMUJ 060855.5+241847	14007	14.75	0.79	0.95	1.84	$2.2^{+0.3}_{-0.3}$	3.1 ± 0.7	19.4 ± 0.7	SM
XMMUJ 060902.5+241952	9003	16.28	1.06	1.81	2.11	$2.7^{+0.3}_{-0.3}$	3.8 ± 0.3	23.4 ± 0.5	BM
XMMUJ 060842.9+242939	43022	15.78	1.01	1.54	2.35	$2.4^{+0.4}_{-0.3}$	5.2 ± 0.9	42.3 ± 3.1	SM
XMMUJ 060903.5+241724	28007	15.95	1.06	0.68	1.96	$2.0^{+0.5}_{-0.3}$	2.0 ± 1.0	22.6 ± 0.5	BM
XMMUJ 060817.8+241225	38028	15.30	0.91	0.91	2.47	$2.7^{+0.3}_{-0.3}$	5.7 ± 0.5	56.1 ± 4.5	SM
XMMUJ 060922.8+242026	7007	11.43	0.20	3.12	3.28	$2.1^{+0.5}_{-0.3}$	3.0 ± 1.0	22.8 ± 3.5	BLM
XMMUJ 060900.5+241200	30018	14.53	0.82	1.08	3.35	$2.3^{+0.5}_{-0.4}$	2.4 ± 0.8	42.8 ± 0.9	SM
XMMUJ 060845.1+241956	19011	14.94	0.93	1.59	1.86	$2.6^{+0.5}_{-0.4}$	2.8 ± 0.5	12.5 ± 0.9	SM
XMMUJ 060913.4+240949	38022	15.49	0.88	3.46	2.73	$2.7^{+0.4}_{-0.4}$	5.9 ± 0.7	$\leqslant$10.0[c]	SM
XMMUJ 060912.4+242453	17010	14.63	0.75	3.12	2.36	$2.1^{+0.7}_{-0.5}$	2.0 ± 2.0	12.5 ± 1.0	SM
XMMUJ 060928.8+242533	46015	15.67	0.92	0.61	2.10	$2.8^{+0.3}_{-0.3}$	5.1 ± 0.5	13.6 ± 1.8	SM
XMMUJ 060841.1+242130	27013	14.86	0.75	0.60	2.39	$3.4^{+0.6}_{-0.7}$	2.0 ± 0.3	11.1 ± 0.5	SM

Notes.
[a] Best-fit power law index.
[b] Model-determined unabsorbed luminosity between 0.2 and 10.0 keV.
[c] Upper-limit $v \sin i$ measurement based on spectral resolution.

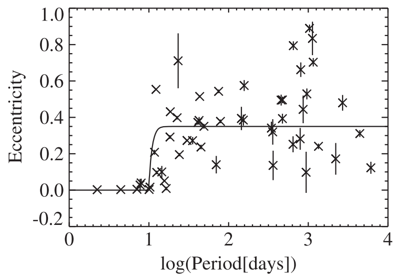

Figure 8. Distribution of orbital eccentricity (e) as a function of the log of the orbital period (P) in days for the M35 main-sequence binary population. The line is the best fit function of the form given in Equation (6) with a CP of 9.9 days.

In order to obtain accurate X-ray luminosities we extract and fit spectra for the 13 X-ray sources. The sources do not have enough counts to carry out model determination, so we fit an absorbed power law (XSPEC models XSPHABS and XSPOWERLAW) to each source. We extract spectra for each source from each camera and fit the spectra simultaneously using *Sherpa*, the data modeling and fitting package in CIAO 4.5 (Fruscione et al. 2006). We use Cstat statistics (Cash 1979) and implement Nelder–Mead simplex optimization (Nelder & Mead 1965). The absorption for each source is fixed to the cluster value of $N_H = 1.159 \times 10^{21}\ \mathrm{cm}^{-2}$. Background spectra are extracted from source-free regions near each X-ray position and are fit simultaneously with the source spectra using an absorbed power law.

Uncertainties in the reported power law spectral slope are given as 1σ errors as calculated by the *Sherpa* task CONF. The X-ray flux uncertainty is found using the task SAMPLE_ENERGY_FLUX. This task randomly samples within the model confidence intervals 1000 times and calculates the resulting flux. The standard deviation of the distribution of fluxes is assumed to be the 1σ flux uncertainty. In Table 9 we present the position (as the *XMM* ID), optical counterpart WOCS ID, optical magnitude and color, and the counterpart separation for the 13 X-ray sources in our sample, as well as the corresponding best fit power law spectral index, unabsorbed X-ray luminosity, $v \sin i$ of the optical counterpart, and the optical counterpart membership classification. The X-ray luminosities are calculated using a cluster distance of 912 pc (Kalirai et al. 2003).

We note there are differences in the source list between this study and the work of Gondoin (2013). The X-ray counterparts for WOCS IDs 43022, 38038, 14007, 19011, 9003, 28007, 46015, and 30018 exist in both studies. Additional X-ray sources with optical counterparts found in the Gondoin (2013) study are at the edges of the instrument field of view, where spurious detections are more likely due to instrument defects. We do not detect an X-ray source at any of those positions. Our identification of X-ray counterparts for WOCS IDs 6021, 7007, 38022, 17010, and 27013 are new matches due to differences in cross-correlation technique and updates in the membership information for these sources. We also note that the spectral extraction and fitting analysis used here is a more robust measurement of X-ray flux that takes into account the instrument response at each source position, rather than applying the flat count-to-flux conversion rate used in previous studies (Gondoin 2013).

5.2. *Origin of X-ray Emission*

Three of the 12 member (BM, SM) or likely-member (BLM) X-ray sources are observed to be binaries with main-sequence primaries. We present orbital solutions for two of these binaries in this paper (WOCS 28007 and WOCS 9003). Both binaries have long period orbits (160 days for 28007 and 800 days for 9003).

We do not yet have an orbital solution for the third system, the BLM WOCS 7007. Early observations indicate it may be a short-period binary, but we require more observations to determine its orbital period. One additional source, WOCS 6021, is also a binary star. We have insufficient observations to determine an orbital solution or membership, and the star is classified as BU. We will continue to observe these two stars.

The observed X-ray emission from SMs or confirmed long-period main-sequence binaries cannot arise from binary interactions. Instead, it is likely linked to stellar rotation. The connection between rotation and X-ray emission is the focus of many papers (e.g., Barnes 2003; Wright et al. 2011; Gondoin 2013), with the fastest rotators in clusters linked to increased X-ray luminosities. Of the 7 X-ray sources with photometric rotation periods determined by Meibom et al. (2009), we find an average period of 1.6 days, compared to 4.5 days for all members in the sample of Meibom et al. (2009). Our $v \sin i$ measurements also indicate that the X-ray counterparts have elevated rotation velocities, with an average $v \sin i = 25.1\ \mathrm{km\ s^{-1}}$ for X-ray counterparts versus $17.2\ \mathrm{km\ s^{-1}}$ for all confirmed cluster members in our sample. Given this evidence, we find it is reasonable to attribute the X-ray emission to stellar activity due to rotation.

We note that the *XMM* observations were designed to detect X-ray binaries, not investigate coronal X-ray emission. With this goal in mind, the detection limit of these observations is above the typical X-ray luminosities associated with stellar activity and therefore detects only a small sample of sources. It is thus of limited utility in exploring the X-ray emission regimes associated with rotation. Gondoin (2013) provide such an analysis of the link between X-ray emission and the rotational properties of these X-ray emitters in M35, albeit with a moderately different sample due to the differences in technique outlined above. We do not do a re-analysis here.

6. TIDAL CIRCULARIZATION

Using our sample of main-sequence binary orbits in M35, we explore the relationship between orbital period and eccentricity. Figure 8 shows the e-log P distribution of binaries in the cluster. The e-log P diagram illustrates that at longer periods, binaries are observed to have a wide range of eccentricities. At very short periods, however, all the binaries have circular orbits. This circularization happens quite abruptly around $P \sim 10$ days.

The circularization of these orbits is due to tidal interactions between the two stars in the binary gradually circularizing the system over the lifetime of the cluster. This theory of tidal circularization predicts that the length of time it takes to circularize a binary strongly depends on the initial separation of the stars. Older clusters should thus have longer circularization periods (CPs) because tidal forces have had time to circularize wider orbits. Due to its young age (~150 Myr), M35 offers a sample of binaries that have only recently left their pre-main-sequence phase. The cluster therefore offers important observational constraints on the early state of main-sequence tidal circularization.

Meibom & Mathieu (2005) determine a tidal CP of $10.2^{+1.0}_{-1.5}$ days in M35 based on 32 binary orbits derived from WOCS RV measurements. Here we revisit their procedure with an expanded sample of 52 orbits.

Meibom & Mathieu (2005) determine a CP by fitting an eccentricity distribution of the form:

$$f(P) = \begin{cases} 0.0 & : P \leqslant P' \\ \alpha(1 - \exp\beta(P' - P))^{\gamma} & : P > P'. \end{cases} \quad (6)$$

Following their procedure, we set $\alpha = 0.35$, the mean eccentricity observed in binaries with $P > 50$ days in the Pleiades, M35, Hyades, M67, and NGC 188; we set $\beta = 0.14$ and $\gamma = 1.0$, the values adopted by Meibom & Mathieu (2005) based on the results of Monte Carlo experiments. We find CP = 9.9 ± 1.2 days, consistent with the results of Meibom & Mathieu (2005). Though our sample has nearly doubled in size from Meibom & Mathieu (2005), we have discovered only four additional binary systems with $P < 50$, the period range most crucial for constraining the CP, and thus our uncertainty is comparable to Meibom & Mathieu (2005).

For a discussion of the evolution of CP with cluster age based on main-sequence binary populations in five open clusters (the Pleides, Hyades, M35, M67, and NGC 188) see Meibom & Mathieu (2005). More recently, Milliman et al. (2014) published an augmented result for the CP as a function of age that includes NGC 6819, an intermediate age (2.5 Gyr) open cluster. Both papers conclude there is an evolution toward larger CP with greater cluster age that is as yet unmatched by any self-consistent tidal evolution theory. Our result for M35 does not change the results reported by these studies.

7. BINARY FREQUENCY

We find a total of 64 BM or BLM out of a total sample of 418 members (SM, BM, BLM). One of these members is a BLM X-ray source outside the WOCS color–magnitude range. Two of these members are binaries that are no longer in the WOCS color–magnitude range after a photometry update (see Section 2). Excluding these stars, we find 61 out of 415 members to be binaries. This yields an observed binary frequency of 15%.

Monte Carlo analysis can give us insight into the our binary detection completeness. Geller & Mathieu (2012) perform such an analysis to correct for incompleteness in NGC 188. They produce a sample of artificial binaries by sampling from a parent distribution based on a well characterized study of field binaries (Raghavan et al. 2010). They sample this distribution at intervals dictated by actual WOCS observations of NGC 188 completed over the course of 14 years. They conclude they detect 88% of binaries with periods under 1000 days, 78% of binaries with periods under 3000 days, and 63% of binaries with periods under 10^4 days. A similar analysis is done by Milliman et al. (2014) for NGC 6819, another WOCS cluster. They find a comparable binary detection percentage of 88% for binaries with periods under 1000 days, 81% for binaries with periods under 3000 days, and 67% for periods less than 10^4 days. The observations of NGC 188 and NGC 6819 are quite similar to those for M35 (though the slightly poorer precision in M35 would have a small impact on the incompleteness), thus we find it reasonable to apply their results to our sample.

Assuming the incompleteness determined in Geller & Mathieu (2012), we find an incompleteness corrected binary frequency of 24% ± 3% (for a 1σ confidence interval) for main sequence binaries in M35 with periods less than 10^4 days. Note that this period limit is important when comparing to results of other studies. Many studies include longer period binaries (10^7–10^8 days) (Eggleton & Tokovinin 2008; Raghavan et al. 2010) and thus find correspondingly larger binary fractions. Our binary frequency is consistent with the binary frequency determined by Geller et al. (2010) for M35 (24% ± 3%). Interestingly, it is also comparable to the main-sequence binary frequency found in NGC 188 and NGC 6819, though those clusters are quite a bit older, and therefore more dynamically evolved. Geller & Mathieu (2012) find a binary frequency in NGC 188 (7 Gyr) of 29% ± 3% and Milliman et al. (2014) determine a binary frequency for NGC 6819 (2.5 Gyr) of 22% ± 3% for main-sequence binaries with periods under 10^4 days. This is consistent with the *N*-body simulations of Geller et al. (2013), which indicate main-sequence binary frequency in this period range shows little evidence of modification by stellar dynamical encounters even after 7 Gyr of dynamical evolution.

8. SUMMARY

In this second paper in a series studying the dynamical state of the young (150 Myr) open cluster M35 we present an updated version of our complete RV database for the cluster. Our sample is selected to cover the range of the M35 main sequence from 0.8 to 1.6 $M_{\odot}$ out to 30′ from cluster center. In the 17 years that we have observed M35, we have gathered ~8000 moderate-precision ($\sigma_i = 0.5$ km s^{-1}) spectra of ~1300 stars. We find 418 of these to be confirmed RV cluster members or likely members.

Within our sample of 418 cluster members or likely members, we detect 64 velocity-variable stars. We present orbital solutions for 52 of these 64 systems, in addition to 28 completed orbital solutions for non-member binaries in our field of view.

We also present X-ray detections in M35 from *XMM-Newton*. We review the data we have on the 12 member optical counterparts of these detections, including three spectroscopic binaries, concluding the detected binary X-ray sources are due to rapid stellar rotation rather than having an origin associated with interacting binaries.

Using this binary sample, we determine the tidal CP of main sequence binaries. We find a CP of 9.9 ± 1.2 days, in agreement with a previous measurement of $10.2^{+1.0}_{-1.5}$ days. We also determine the main-sequence binary frequency to be 24% ± 3% for binaries out to periods of less than 10^4 days. Interestingly, this frequency is consistent with the binary frequencies found in the much older clusters NGC 188 and NGC 6819, potentially indicating little dynamical evolution of binary frequency.

The authors would like to thank the staff of the WIYN Observatory for their assistance obtaining the tens of thousands of spectra WOCS has obtained over the years. Thanks to the anonymous referee for comments on this paper. We would also like to thank the many generations of graduate and under-graduate students who have helped with observations and data reduction, with special gratitude to K. Milliman and B.

Tofflemire for their input on this project. Thanks to Tom Finzell for his work on the binary orbits in this paper, and to Aisha Mahmoud for her work on the *XMM* X-ray sources. This work was funded by the National Science Foundation grant AST-0908082 to the University of Wisconsin-Madison. A.M.G. is funded by the National Science Foundation Astronomy and Astrophysics Postdoctoral Fellowship No. AST-1302765.

REFERENCES

Barnes, S. A. 2003, ApJL, 586, L145
Barrado y Navascués, D., Deliyannis, C. P., & Stauffer, J. R. 2001a, ApJ, 549, 452
Barrado y Navascués, D., Stauffer, J. R., Bouvier, J., & Martín, E. L. 2001b, ApJ, 546, 1006
Cash, W. 1979, ApJ, 228, 939
Cudworth, K. M. 1971, AJ, 76, 475
Eggleton, P. P., & Tokovinin, A. A. 2008, MNRAS, 389, 869
Fruscione, A., McDowell, J. C., Allen, G. E., et al. 2006, Proc. SPIE, 6270, 62701V
Geller, A. M., Hurley, J. R., & Mathieu, R. D. 2013, AJ, 145, 8
Geller, A. M., & Mathieu, R. D. 2011, Natur, 478, 356
Geller, A. M., & Mathieu, R. D. 2012, AJ, 144, 54
Geller, A. M., Mathieu, R. D., Braden, E. K., et al. 2010, AJ, 139, 1383
Geller, A. M., Mathieu, R. D., Harris, H. C., & McClure, R. D. 2008, AJ, 135, 2264
Geller, A. M., Mathieu, R. D., Harris, H. C., & McClure, R. D. 2009, AJ, 137, 3743
Gondoin, P. 2013, A&A, 556, A14
Hole, K. T., Geller, A. M., Mathieu, R. D., et al. 2009, AJ, 138, 159
Howell, S. B., Sobeck, C., Haas, M., et al. 2014, PASP, 126, 398
Hu, J.-H., Ip, W.-H., Zhang, X.-B., et al. 2005, ChJAA, 5, 356
Hurley, J. R., Pols, O. R., Aarseth, S. J., & Tout, C. A. 2005, MNRAS, 363, 293
Kalirai, J. S., Fahlman, G. G., Richer, H. B., & Ventura, P. 2003, AJ, 126, 1402
Leonard, P. J. T., & Merritt, D. 1989, ApJ, 339, 195
Mathieu, R. D. 1983, PhD thesis, Univ. California Berkeley
Mazeh, T., & Zucker, S. 1994, Ap&SS, 212, 349
McNamara, B., & Sekiguchi, K. 1986, AJ, 91, 557
McNamara, B. J., Harrison, T. E., McArthur, B. E., & Benedict, G. F. 2011, AJ, 142, 53
Meibom, S., & Mathieu, R. D. 2005, ApJ, 620, 970
Meibom, S., Mathieu, R. D., & Stassun, K. G. 2006, ApJ, 653, 621
Meibom, S., Mathieu, R. D., & Stassun, K. G. 2007, ApJL, 665, L155
Meibom, S., Mathieu, R. D., & Stassun, K. G. 2009, ApJ, 695, 679
Milliman, K. E., Mathieu, R. D., Geller, A. M., et al. 2014, AJ, 148, 38
Nelder, J. A., & Mead, R. 1965, CompJ, 7, 308
Raghavan, D., McAlister, H. A., Henry, T. J., et al. 2010, ApJS, 190, 1
Rhode, K. L., Herbst, W., & Mathieu, R. D. 2001, AJ, 122, 3258
Sarrazine, A. R., Steinhauer, A. J. B., Deliyannis, C. P., et al. 2000, BAAS, 32, 1461
Steinhauer, A., & Deliyannis, C. P. 2004, ApJL, 614, L65
Sung, H., & Bessell, M. S. 1999, MNRAS, 306, 361
van den Berg, M., Verbunt, F., Tagliaferri, G., et al. 2013, ApJ, 770, 98
von Hippel, T., Steinhauer, A., Sarajedini, A., & Deliyannis, C. P. 2002, AJ, 124, 1555
Watson, M. G., Schröder, A. C., Fyfe, D., et al. 2009, A&A, 493, 339
Williams, K. A., Bolte, M., & Koester, D. 2004, ApJL, 615, L49
Williams, K. A., Bolte, M., & Koester, D. 2009, ApJ, 693, 355
Williams, K. A., Liebert, J., Bolte, M., & Hanson, R. B. 2006, ApJL, 643, L127
Wright, N. J., Drake, J. J., Mamajek, E. E., & Henry, G. W. 2011, ApJ, 743, 48